

AN INCREMENTAL MODULAR MDO FRAMEWORK FOR HYDROGEN-ELECTRIC POWERTRAIN SIZING AND INTEGRATION IN GENERAL AVIATION AIRCRAFT

Pablo Moreno-Escolástico, Marco Raiola, Rodrigo Castellanos & Andrea Cini

Department of Aerospace Engineering, Universidad Carlos III de Madrid, Leganés, Spain

Abstract

The design of hydrogen-fuelled electric propulsion systems for sustainable aviation aircraft is governed by strong multidisciplinary couplings between power generation, thermal management, aerodynamics and airframe integration which conventional sequential sizing approaches cannot adequately address. This paper presents a physics-based Multidisciplinary Design Optimisation (MDO) framework for the integrated sizing of fully electric powertrains simultaneously driven by hydrogen fuel cells and batteries. The optimisation is implemented in OpenMDAO and solved using gradient-based algorithms. The framework concurrently sizes the fuel cell system, electric motor, battery pack, Thermal Management System (TMS), air intake, and Balance of Plant (BoP) components within a single coupled optimisation environment, capturing interdisciplinary interactions such as the trade-off between fuel cell operating voltage, heat generation waste, and cooling drag. The framework is validated through two application cases. First, a design methodology comparison for the sizing requirement of 100 kW max power at sea-level demonstrates that the coupled MDO formulation achieves a 19.1% reduction in total mass related to a sequential approach, driven by a non-intuitive fuel cell–TMS trade-off structurally inaccessible for decoupled methods. Second, the framework is applied to the sizing of a 1 MW hydrogen fuelled electric replacement for a single powerplant of the Dornier Do-328 regional aircraft, yielding a total dry powertrain mass of 1,819 kg and a mission hydrogen consumption of 57.7 kg over a 280 nm range. The results demonstrate that physics-based coupled optimisation is necessary, not merely preferable, for hydrogen-electric propulsion design, and establish a robust foundation for certifiable preliminary design of sustainable aviation powertrains.

Keywords: Multidisciplinary Design Optimisation, Hydrogen-electric, Propulsion System, Sustainable Aviation

1. Introduction

Hydrogen-fuelled electric and hybrid-electric propulsion systems have attracted increasing interest as sustainable alternatives for general aviation and regional transport [1], driven by international agreements, decarbonisation programmes aiming at a climate neutrality targets by 2050 [2, 3]. While fully battery-electric propulsion offers zero in-flight emissions, the limited specific energy of current battery technologies restricts their applicability to larger aircraft categories [4]. Fuel cell-based hydrogen-electric systems offer a compelling alternative, combining hydrogen high specific energy with zero direct emissions. For general and regional aviation applications, fuel cell-battery hybrid fully electric configurations are particularly attractive: the fuel cell provides efficient steady-state power while the battery covers transient peak demands, improving overall system responsiveness and operative envelope.

The design of such systems is inherently multidisciplinary. Fuel cell operating conditions directly determine heat rejection requirements, driving TMS sizing; heat exchanger integration introduces aerodynamic drag penalties affecting propulsive efficiency and Balance of Plant (BoP) components

impose significant mass and parasitic power penalties becoming primary design drivers. Local design decisions, therefore, propagate across disciplines, generating non-intuitive system-level trade-offs. Despite these intrinsic coupled interactions, most existing conceptual sizing methodologies rely on sequential procedures and low-fidelity empirical correlations [5], treating subsystems in isolation and architecturally preventing the resolution of cross-disciplinary trade-offs.

This work presents a fully integrated, physics-based MDO framework for the coupled sizing and optimisation of hydrogen-electric powertrains in sustainable aviation aircraft. Implemented in OpenMDAO and solved using gradient-based optimisation, the framework concurrently sizes the fuel cell system, battery, electric motor, TMS and air intake through coupled performance, sizing, and mass models, explicitly resolving BoP effects and enforcing power, thermal, and aerodynamic constraints at the conceptual design level. Unlike prior approaches, the framework explicitly resolves the cross-disciplinary interactions between fuel cell operating point, waste heat generation, cooling drag and auxiliary power consumption, enabling the identification of system-level trade-offs that are inaccessible to sequential methods.

2. Physics-based Multidisciplinary Models

The propulsion system subsystem models are implemented as modular components within the OpenMDAO framework [6], enabling efficient total sensitivity computation through analytic partial derivatives and the automated assembly of system-level Jacobians required for gradient-based optimisation. Each subsystem model is developed and verified independently before integration within the coupled multidisciplinary environment, following the incremental strategy described in Section 3.. The overall propulsion system architecture and subsystem interconnections are illustrated in Figure 1. An important parameter in this architecture is the hybridisation factor,

$$HF = \frac{P_{fuel\,cell}}{P_{fuel\,cell} + P_{batt}} \tag{1}$$

defining the power split between the fuel cell and battery. It constitutes a key design variable in the optimisation. In this way, the tool enables the analysis and optimisation of a wide variety of combinations with the present architecture. Additionally, having two power sources allows the fuel cell to operate at continuous optimal conditions, while the battery supplies extra power when rapid variations are required.

The following subsections describe the models for the electric motor and propeller, fuel cell system, battery pack, TMS and air intake duct.

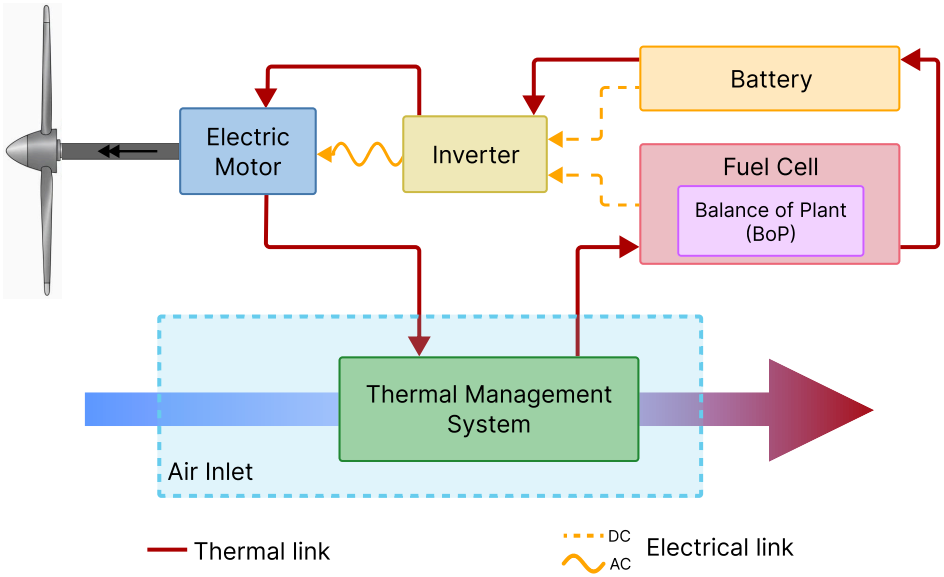


Figure 1 – Global propulsion system architecture and subsystem interconnections

2.1 Electric Motor

The electric motor is modelled as a radial flux surface-mounted Permanent Magnet Synchronous Motor (PMSM) following the analytical sizing methodology of Bahrs et al. [7]. The model is capable of predicting motor dimensions, efficiency, losses and mass from the required shaft power and rotational speed. It explicitly links motor geometry, operating conditions, and loss mechanisms to performance, enabling the optimiser to capture the impact of motor design decisions on electrical power demand, thermal generation, and system mass.

Machine dimensions are derived from analytical electromagnetic loading relations relating the required mechanical power to the air-gap geometry, magnetic loading, and electric loading [7, 8]. The relative motor length λ is defined as follows

$$\lambda = \frac{l}{d_{gap}} \frac{N_p}{\pi} \tag{2}$$

where l is the rotor length, d_{gap} the air-gap thickness, and N_p the number of magnet poles, is treated as a primary design variable. A key internal coupling arises from the effective air-gap thickness, which depends on both the mechanical clearance and the carbon-fibre retaining sleeve required to withstand centrifugal loads, directly linking structural and electromagnetic sizing. Rotor, stator and winding geometries are subsequently derived from the electromagnetic dimensions using analytical and semi-empirical relations.

Motor efficiency is evaluated through a detailed power loss breakdown,

$$P_{loss} = P_j + P_{Fe} + P_{mech} + P_{add} \tag{3}$$

accounting for copper losses from winding resistance and operating current (P_j), iron losses from hysteresis and eddy-current effects (P_{Fe}), mechanical windage losses (P_{mech}), and additional stray losses (P_{add}). The resulting efficiency,

$$\eta = \frac{P_{shaft}}{P_{shaft} + P_{loss}} \tag{4}$$

is treated as an implicit variable within the non-linear solution process, ensuring consistency between motor performance and powertrain-level energy balances. Motor mass is estimated from the geometry and material properties of the principal components: stator, rotor, windings, permanent magnets, retaining sleeve, and shaft. This provides direct coupling between electromagnetic sizing, structural requirements, and system mass.

Design Variables and Constraints

The principal motor design variables are the relative motor length λ, the copper fill factor k_{fill} and the magnet thickness h_{mag}. The rotational speed may either be prescribed by the propeller architecture or treated as an additional design variable.

Geometric constraints are imposed on motor size to ensure aircraft integration compatibility and manufacturing feasibility, while electromagnetic and structural integrity constraints guarantee feasible operating conditions.

2.2 Fuel Cell System

The electrical power generation subsystem is based on a Proton Exchange Membrane Fuel Cell (PEMFC) architecture, following the semi-empirical sizing methodology of O'Hayre et al. [9], adapted for aerospace applications by Datta [10]. The model explicitly relates stack performance to operating conditions, current density, reactant pressure and temperature, predicting stack voltage, electrical power, reactant mass flow rates, heat rejection requirements and system size and mass.

Cell voltage, V_{cell}, is computed using a semi-empirical polarisation curve accounting for reversible voltage generation and activation, ohmic, and concentration losses,

$$V_{cell} = E_{Nernst} - \eta_{act} - \eta_{ohm} - \eta_{conc} \tag{5}$$

The reversible voltage (E_{Nerst}) is evaluated from the Nernst equation [10], incorporating reactant partial pressures and operating altitude. Activation losses (η_{act}) follow a Butler-Volmer formulation, while ohmic (η_{ohm}) and concentration losses (η_{conc}) account for membrane resistance and reactant transport limitations, respectively [10].
Additionally, the model includes edge cell penalty, accounting for the suboptimal operation of the cells near both stack ends.

Balance of Plant

High-altitude operation requires pressurised cathode air to maintain adequate oxygen availability and prevent voltage degradation [11, 12]. An electrically driven centrifugal compressor provides the required pressure ratio, with its power consumption and thermal load modelled as functions of altitude and fuel cell airflow demand. Compressor power is treated as a parasitic load directly coupled to the system power balance. A membrane humidifier maintains adequate hydration under low-humidity high-altitude conditions; its mass is estimated from the required membrane area following Datta [10]. Both components are incorporated within the overall power and mass balances, constituting critical design drivers rather than secondary subsystems.
Hydrogen storage is modelled using a gravimetric index approach, with tank mass estimated as a function of total required hydrogen mass and assumed storage technology. The hydrogen inventory accounts for both nominal mission consumption and operational reserve margins covering contingencies such as holding patterns and diversion procedures.

Design Variables and Constraints

The fuel cell model is integrated within the propulsion system optimisation framework through three primary design variables: stack active area (A), number of cells (N_{cells}), and total stack current (I_{tot}). These variables determine the electrochemical operating point, stack dimensions, power capability, reactant consumption, and thermal generation.
Several physical and operational constraints are imposed during optimisation. Geometric constraints are applied to ensure compatibility with the available installation volume within the propulsion architecture. In addition, the operating current density is constrained below the cell limiting-current region to prevent excessive concentration losses and reactant starvation.
A minimum cell-voltage constraint is also enforced to avoid operating conditions associated with accelerated degradation mechanisms, including catalyst degradation and membrane ageing [9, 11]. This constraint ensures that all feasible solutions remain within representative feasible operating conditions for long-term PEMFC operation.

2.3 Battery

The battery pack is modelled using an equivalent-circuit formulation derived from Doyle et al. [13], predicting terminal voltage, discharge current, power capability, and electrical efficiency as functions of pack configuration and operating conditions. The pack is defined by the number of cells in series and parallel, which set the voltage level, current capability and energy storage capacity. Battery pack power demand is directly coupled to the hybridisation factor HF (Equation (1)) and the powertrain power-management strategy [4, 14].
At the critical design point, a power-driven sizing methodology is adopted, consistent with the Single Design Point (SDP) formulation: battery capacity is determined by the maximum allowable discharge rate, operating in the power-limited region of the Ragone diagram [15, 16], where specific power governs the design. The effective usable capacity is corrected for high-current operation using Peukert's relationship [17]. During mission analysis, an energy-based sizing is additionally applied, where capacity requirements are determined from the mission power profile and hybridisation strategy, capturing the trade-off between power capability, energy storage and battery mass.
Battery mass is estimated from the required energy capacity and cell specific energy, with pack-level contributions from structural enclosure, battery management systems and integration hardware [18, 19]. Thermal losses are dominated by Joule heating from internal cell resistance, with the resulting heat generation driving directly to the TMS sizing. This interaction becomes particularly significant

during high-power phases where discharge rate, thermal generation, and propulsion system performance are simultaneously affected.

Design Variables and Constraints

The battery design variables are the number of cells connected in series, n_s, and in parallel, n_p. n_s primarily controls the pack voltage, while n_p determines the current capability and energy storage capacity. Additionally, the hybridisation factor HF determines the power sharing between the battery and fuel cell.

Additionally, operational constraints are imposed to ensure safe and feasible battery operation. These include maximum allowable discharge-rate limits, minimum terminal voltage requirements and energy-capacity constraints. Collectively, these constraints guarantee that the battery can satisfy the required power demand while remaining within acceptable operating conditions throughout the mission.

2.4 Propeller

Propeller performance is evaluated using a Blade Element Momentum Theory (BEMT) formulation combining Blade Element Theory (BET), which resolves the aerodynamics at each radial section, with one-dimensional momentum theory applied to annular streamtubes [20, 21]. Section lift and drag coefficients are obtained from NFoil [22], an efficient panel-based subsonic airfoil solver, and three corrections are applied to the two-dimensional polars prior to the BEMT iteration: the Prandtl tip-loss factor for finite-blade effects, the Corrigan-Schillings stall-delay correction for rotational augmentation [23] and a Joukowsky inter-blade interaction correction for mutual induction effects [24]. At each radial station, the inflow angle and effective relative velocity are obtained iteratively, and sectional loads are integrated numerically over the blade span to yield total rotor thrust and shaft power. The model additionally predicts the disk-plane flow conditions passed to the air intake module as upstream boundary conditions, ensuring full consistency between the propulsive and thermal-aerodynamic subsystems.

2.5 Thermal Management System

The TMS removes internally generated heat by the fuel cell system, electric motor, battery pack, and power electronics which is a critical design driver in electrified propulsion architectures where no exhaust stream is available for heat dissipation [25, 26]. The architecture follows the liquid-cooled concept of Brelje et al. [25], comprising component-level cold plates, a compact air-cooled heat exchanger, a coolant circulation pump and a reservoir. The total thermal load,

$$\dot{Q}_{gen,tot} = \sum_{i=1\ldots N} \dot{Q}_i \tag{6}$$

is obtained from the summation of individual subsystem model contributions, enforced through a global thermal balance constraint ensuring sufficient heat rejection at the design condition. Heat extraction from each component is represented through a lumped-parameter cold plate model. For SDP analyses thermal equilibrium is assumed, while transient mission-level analyses additionally account for transient behaviour through component thermal capacitance models.

Heat rejection to the environment is performed through a compact Offset-Strip-Fin (OSF) heat exchanger [27, 28], selected for its high surface-area density and favourable heat-transfer-to-weight ratio. Thermal performance is evaluated using the NTU-effectiveness method with the Manglik-Bergles correlations [28], and pressure losses are estimated following Kays and London [27]. Since the cold-side airflow is supplied through the cooling inlet (Section 2.6), heat-exchanger pressure losses directly couple thermal management to aerodynamic internal drag, one of the primary cross-disciplinary interactions in the framework. The pump is sized from the total circuit pressure losses and its power is treated as a parasitic electrical load within the system power balance, enabling the optimiser to perform a trade-off between coolant flow rate, thermal performance and auxiliary power consumption.

The dissipation of the total generated heat by the propulsion system at the prescribed operating condition is ensured by enforcing thermal equilibrium.

Design Variables and Constraints

The principal TMS design variables are the heat-exchanger geometric parameters, including the number of channel layers and streamwise channels, together with the coolant and cooling-air mass flow rates. These variables directly influence heat-rejection capability, system mass, pressure losses and cooling drag.

Heat exchanger integrability and manufacturability is ensured by imposing geometrical constraints on the size. Additional constraints may be imposed on maximum component temperatures and allowable pressure losses to ensure safe and feasible operation of the propulsion architecture.

2.6 Air Intake Modelling

The air intake is modelled using a physics-based one-dimensional (1D) framework predicting the thermo-fluid dynamic state of the flow through a ducted heat exchanger installed in the propeller wake. Rather than relying on CFD, the module maps the physical domain onto a parametrised 1D streamtube, coupling compressible flow theory for internal duct aerodynamics with empirical models for external nacelle drag. Dissipated heat and pressure loss data are received directly from the TMS heat exchanger module, ensuring consistency between duct aerodynamics and thermal performance throughout the iterative solution process. Figure 2 shows the flow physical domain, spanning from the propeller disk to the nozzle exit section, where the heat exchanger can be mounted with an angle α_{HEX}.

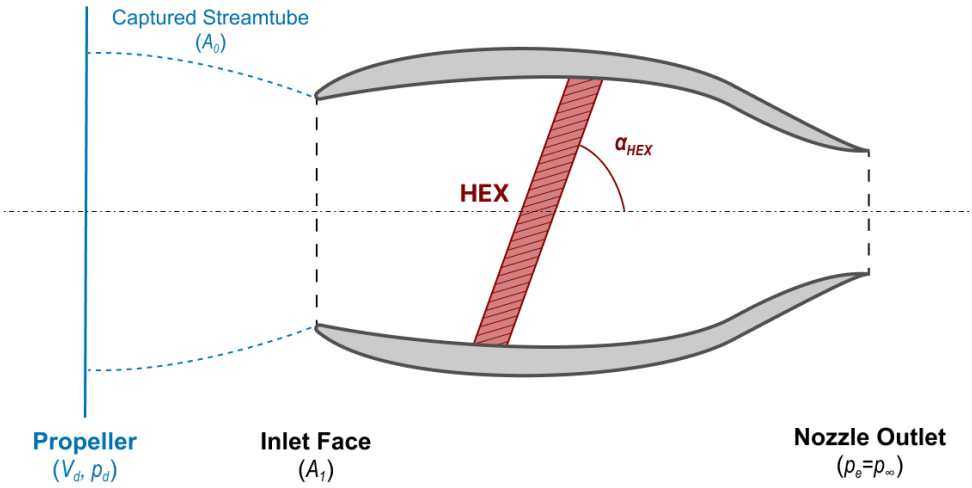


Figure 2 – 1D domain schematic: propeller to nozzle exit

Propeller Wake Capture

The inlet boundary conditions are set by the flow state immediately downstream of the propeller rather than the ambient free stream. The disk-averaged axial velocity is obtained from the propeller model (Section 2.4) as the local axial velocity averaged across the rotor annulus area, and the disk-averaged static pressure is derived by combining a Bernoulli relation upstream of the disk with the thrust-induced pressure jump across it. These quantities, together with the ambient temperature, fully define the stagnation pressure $P_{0,wake}$ and stagnation temperature $T_{0,wake}$ passed to the inlet module as upstream boundary conditions. For lower-fidelity analyses, wake conditions may alternatively be estimated from classical Actuator Disk Theory [29].

The transition from the propeller wake to the physical duct is regulated by the ratio of a far-upstream streamtube of area A_0, to the fixed inlet area A_1, through the Capture Area Ratio $CAR = A_0/A_1$. The pre-entry process is treated as isentropic and adiabatic, conserving stagnation pressure and temperature to the inlet face. The inlet Mach number M_1 is obtained by numerical root-finding on the exact isentropic area-Mach relation [30]. From this relation isentropic equations yield static pressure, density, and temperature at the inlet plane. For cases where $A_0 < A_1$, the leading-edge suction force

fully recovers the additive spillage drag, rendering net spillage drag negligible for well-contoured nacelles [31]. External losses are therefore evaluated exclusively as friction and form drag over the wetted nacelle surface.

One-Dimensional Compressible Internal Flow

Internal flow is governed by simultaneous area change, viscous wall friction, heat addition from the heat exchanger, and core blockage. These effects are concurrently captured through the Generalised 1D Compressible Flow formulation of Zucrow and Hoffman [32], yielding the following Mach number evolution,

$$\frac{dM}{M} = -\frac{\psi}{1-M^2}\frac{dA}{A} + \frac{\gamma M^2 \psi}{2(1-M^2)}\left[4f\frac{dx}{D_e} + \frac{2\,d\mathscr{D}}{\gamma p A M^2}\right] + \frac{(1+\gamma M^2)\psi}{2(1-M^2)}\frac{dT_0}{T_0} \tag{7}$$

where $\psi = 1 + \frac{\gamma-1}{2}M^2$ is the compressibility factor, simultaneously capturing area-driven acceleration, friction- and blockage-induced choking tendency and the Rayleigh heating effect. The $(1-M^2)$ at denominator in every influence coefficient represents the sonic singularity at $M=1$, providing the physical justification for the Mach number constraint detailed in Section 2.6. The heat exchanger introduces a total internal blockage force,

$$\mathscr{D} = A\left(\Delta p_{HEX} + \rho V^2 \sin\alpha_{HEX}\right) \tag{8}$$

accounting for both core pressure drop and momentum loss from the heat exchanger tilt angle α_{HEX}. Both Δp_{HEX} and dQ/dx are supplied by the TMS module at every integration step. The governing Ordinary Differential Equations (ODEs) are integrated using a Runge-Kutta scheme over eight state variables, Mach number, static pressure, density, static temperature, velocity, stagnation pressure, impulse function, and entropy. Friction is evaluated via the Haaland and Colebrook–White equations [33]. The streamtube capture area A_0 is determined by a shooting method enforcing the Kutta condition at the nozzle exit.

External Nacelle Drag

External nacelle drag, $\mathscr{D}_{nacelle}$, is evaluated following the component build-up methodology of Raymer [34],

$$\mathscr{D}_{nacelle} = q_\infty S_{wet} C_f FF \tag{9}$$

where $q_\infty = \frac{1}{2}\rho_\infty V_\infty^2$ is the dynamic pressure, S_{wet} is the wetted nacelle area, C_f the compressible skin friction coefficient, and FF the form factor for pressure drag from nacelle curvature. The total ducted-system drag, combining internal momentum losses and external nacelle drag, follows from the nozzle exit momentum balance,

$$\mathscr{D}_{total} = -\dot{m}(V_e - V_0) - (p_e - p_0)A_e + \mathscr{D}_{nacelle} \tag{10}$$

where $\dot{m}$ is the air mass flow rate, and the subindex 0 denotes the properties at section A_0 and e at nozzle exhaust section.

Design Variables and Constraints

The internal geometry is parametrised into three longitudinal segments characterised by different flows: an inlet diffuser, a constant-area heat exchanger core section, and a nozzle. The design variables are the polynomial coefficients defining the area profiles of the inlet diffuser and nozzle, together with the nacelle physical length $L_{nacelle}$. The inlet section length is fixed at $L_{inlet} = 0.4\,m$ given its low sensitivity within the optimisation. Several constraints bound the design space:

- **Aerodynamic singularity:** a strict upper bound on the local Mach number is enforced at every streamwise section to prevent the internal flow from reaching the Zucrow singularity ($M=1$), ensuring fully subsonic operation and preserving the physical validity of the 1D model throughout.

- **Diffuser angle limit:** an implicit bound on the streamwise area expansion rate is imposed to prevent adverse pressure gradients and boundary layer separation, which cannot be captured within the 1D framework.
- **Geometric bounds:** minimum and maximum limits on total duct length and nozzle exit area ensure geometric proportionality with respect to the propeller disk and heat exchanger core.
- **Geometric continuity:** contour (C^0) and tangential (C^1) continuity are enforced at each junction between adjacent polynomial segments to eliminate spurious internal flow discontinuities and ensure manufacturability.

3. MDAO framework

The physics-based subsystem models described in Section 2. are integrated within a unified optimisation environment built in OpenMDAO [6]. The modular software architecture enables a flexible definition of the propulsion system layout and supports the progressive integration of additional disciplinary models and optimisation capabilities without modifying the overall framework structure. Unlike low-fidelity conceptual sizing approaches based on fixed efficiencies or empirical correlations [5], the coupled formulation explicitly resolves the cross-disciplinary interactions governing hydrogen-electric propulsion performance, enabling the identification of non-intuitive system-level trade-offs that are structurally unreachable to conventional sequential sizing methodologies.
The framework addresses two subsequent optimisation problems, following an incremental development strategy, as illustrated in Figure 3. First, a SDP powertrain sizing optimisation establishes the baseline propulsion system configuration under the critical operating design condition. Subsequently, a mission-level energy management optimisation evaluates and optimises the power-sharing strategy over the full flight envelope, verifying that the sized powertrain remains feasible and efficient across all mission phases. This two-stage approach mitigates the risk of obtaining solutions which are optimal at the design point but infeasible or inefficient during realistic mission operation.

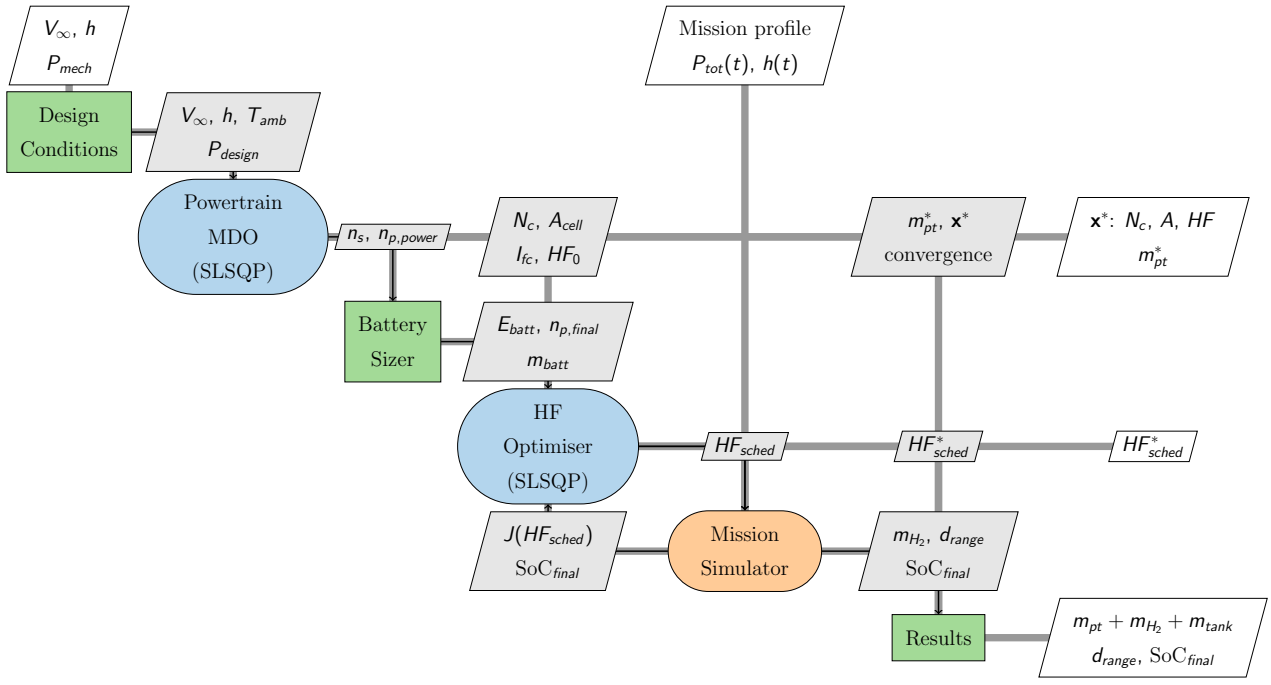


Figure 3 – Powertrain and mission integrated optimisation XDSM diagram

3.1 Powertrain Sizing Optimisation

The powertrain sizing problem is cast as a single-level, single-loadcase minimum-mass formulation where all subsystem models are simultaneously active and share a common set of design variables,

residuals, and constraints. The objective is to minimise the total propulsion system mass as summation of different contributions.

$$\min_{\mathbf{x}} \; m_{sys} = m_{mot} + m_{\mathrm{FCS}} + m_{TMS} + m_{batt} + m_{inv} + m_{inlet} \tag{11}$$

Gradient-based optimisation is performed using the Sequential Least Squares Programming (SLSQP) algorithm, enabling efficient convergence while enforcing two global coupling residuals: power balance, requiring that the net output power equals the demanded shaft power after all parasitic losses; and thermal balance, requiring that the heat generated is dissipated to keep components at safe operational conditions. These are supplemented by component-level feasibility constraints on minimum cell voltage, battery discharge rate, internal duct Mach number, and geometric integration limits. The aforementioned complete set of design variables $\mathbf{x}$, together with the subsystem-level constraints, are gathered in Table 1.

Subsystem	**Design Variables**	**Constraints**
Electric Motor	Relative motor length, λ	Geometric integration limits
	Copper fill factor, k_{fill}	Structural integrity
	Magnet thickness, h_{mag}	
Fuel Cell System	Number of cells, N_c	Minimum cell voltage
	Active cell area, A_{cell}	Maximum current density
	Total stack current, I_{fc}	Geometric integration limits
Battery Pack	Cells in series, n_s	Maximum discharge rate
	Cells in parallel, n_p	Minimum terminal voltage
	Hybridisation factor, HF	State of Charge limits
TMS	Number of layers, n_t	Thermal equilibrium
	Spanwise channels, n_w	Geometric integration limits
	Streamwise channels, n_l	Component maximum temperature
	Coolant mass flow rate, $\dot{m}_{cool}$	Maximum pressure losses
	Cooling-air mass flow rate, $\dot{m}_{air}$	
Air Intake	Diffuser polynomial coefficients, c_1	Maximum internal Mach number
	Nozzle polynomial coefficients, c_2	Diffuser angle limit
	Nacelle length, $L_{nacelle}$	Geometric bounds
		Geometric continuity (C^0, C^1)

Table 1 – Design variables and constraints of the SDP sizing optimisation. Constraints in grey have not been implemented in the presented results, but can be implemented

3.2 Mission Energy Management Optimisation

Following the powertrain sizing, the mission analysis module optimises the energy management strategy over a complete flight mission, accounting for variations in power demand, altitude and atmospheric conditions. The mission is represented as a sequence of flight segments: take-off, climb, cruise, descent, and landing. Each one is characterised by its duration, altitude, airspeed, and required propulsive power. Atmospheric conditions are computed using the International Standard Atmosphere (ISA) model [35] and propagated consistently throughout all subsystem models.

For hybrid fuel cell-battery architectures, the power demand at each mission point is distributed between the two energy sources via the hybridisation factor (Equation (1)), which may be held constant or allowed to vary between flight segments. In the mission optimisation formulation, the optimiser determines the power-sharing schedule minimising the composite objective, J,

$$J = w_1 J_{H_2} + w_2 J_{batt} + w_3 J_{deg} + w_4 J_{dyn} \tag{12}$$

combining mission hydrogen consumption, battery energy expenditure, and penalty terms discouraging excessive battery loading and rapid fuel cell power variations. Battery energy expenditure is converted into an equivalent hydrogen cost through an Equivalent Consumption Minimization Strategy (ECMS) formulation [36], ensuring commensurability between the two energy sources. The durability and dynamic penalties on the battery discharge and fuel cell transient behaviour promote operating conditions compatible with long-term component life while maintaining efficient mission performance while preventing rapid ageing.

The optimisation is constrained by battery State of Charge (SoC) limits throughout the mission to prevent electrochemical degradation, together with a minimum reserve-energy requirement at the end of flight. Mission-level hydrogen consumption is obtained by integrating the instantaneous fuel consumption rate over the complete profile, while battery utilisation is tracked through the SoC evolution. The resulting optimised hybridisation schedule identifies not only the most efficient operational strategy for the sized powertrain but also verifies that power, thermal and energy constraints are satisfied across the full flight envelope.

4. Results

Two application cases for the framework are presented below. First, a comparison between sequential and coupled optimisation for an arbitrary case is performed, pinpointing the main differences. Then, the tool is used to perform the sizing of a real powerplant case, performing the optimisation of the equivalent of one of the powerplants propelling the Dornier-328 aircraft together with a mission optimisation.

4.1 Coupled vs. Sequential Optimization Comparison

The case selected for this comparison corresponds to a 100 kW take-off at sea-level design point operated by fuel cell-only, that is, with a hybridisation factor $HF = 1$. In this case the full shaft power demand is met exclusively by the fuel cell system with no battery contribution. To assess the benefit of the fully coupled MDO formulation, the powertrain sizing problem is solved under two alternative optimisation architectures and the resulting system mass breakdowns are compared. The first architecture solves the full multidisciplinary problem simultaneously, treating the electric motor, fuel cell system, TMS and inlet duct as a single coupled system with a shared objective of minimum total mass. The drag penalty imposed by the air inlet is also considered. In this formulation, the aerodynamic drag penalty of the inlet duct enters the objective function directly as a propulsive fuel penalty. That penalty is computed from the additional shaft power required to overcome the inlet-induced drag increment over the design mission. This ensures that inlet mass and aerodynamic drag are simultaneously minimised by the optimiser. The second architecture solves each discipline in sequence: motor $\rightarrow$ fuel cell system $\rightarrow$ TMS $\rightarrow$ inlet duct. There, each step minimises the mass of its own subsystem and passes its outputs downstream as fixed boundary conditions. The inlet drag penalty is considered within the objective function as for the coupled optimisation. To examine how the sequential solution evolves when cross-discipline feedback is introduced, the sequential procedure is repeated for a second pass in which the drag increment produced by the inlet duct is fed back as an additional shaft-power requirement at the start of the new pass.

Table 2 and Figure 4, lists and displays the resulting powertrain mass breakdowns in terms of the total stacked mass and the individual component contributions for each optimisation architecture. The fully coupled optimiser yields a total system mass of 184.1 kg. The one-pass sequential approach produces 219.3 kg, a penalty of 35.2 kg (+19.1%). The second sequential pass, rather than recovering this gap, increases the mass further to 222.8 kg, corresponding to a penalty of 38.7 kg (+21.0%) compared to the coupled solution.

The primary source of the optimum mass gap is a cross-disciplinary trade-off between the fuel cell operating point and TMS size which is structurally unreachable by the sequential approach. The coupled optimiser converges to a mean cell voltage of $V_{cell} = 0.538$ V, compared to 0.500 V in the sequential case. Operating at a higher cell voltage reduces the current density, cutting ohmic and

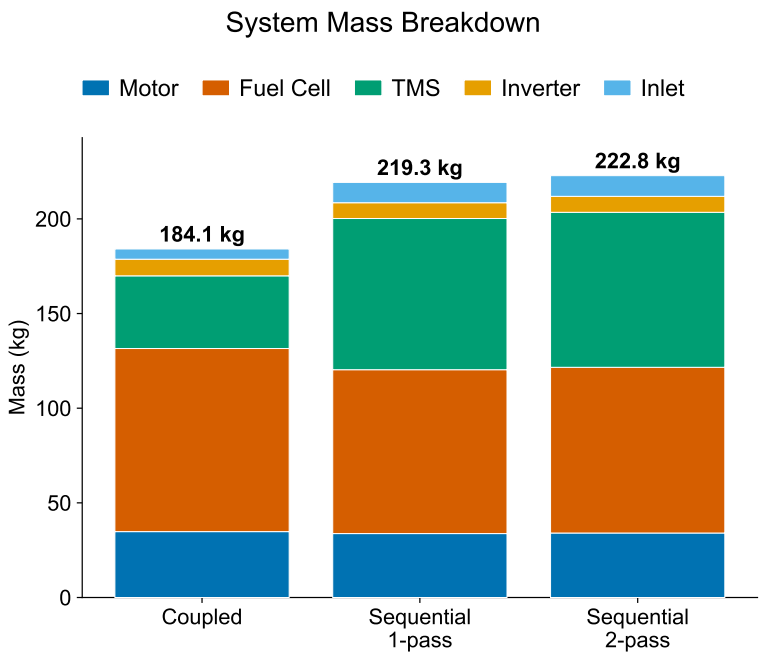


Figure 4 – System mass breakdown by optimization architecture

Architecture	Motor	FC System	TMS	Inverter	Inlet	**Total**	δ
Coupled MDO	34.8	96.7	38.4	8.8	5.4	**184.1**	-
Sequential 1-pass	33.8	86.6	79.9	8.3	10.7	**219.3**	$+19.1\%$
Sequential 2-pass	34.1	87.5	81.9	8.4	10.9	**222.8**	$+21.0\%$

Table 2 – System mass breakdown by optimisation architecture in kg

activation losses and lowering the dissipated heat rate. Consequently, the coupled TMS requires a heat exchanger with a total volume of 0.077 m^3, smaller than one-third of the 0.199 m^3 exchanger produced by the sequential approach. The fuel cell stack incurs a mass penalty of 10.1 kg, but the TMS shrinks by 41.5 kg, yielding a net subsystem saving of 31.4 kg. This trade is invisible to the sequential approach: the fuel cell optimiser minimises only stack mass, driving the cell voltage to its lower feasibility limit and consequently maximising the heat generation.

A secondary coupling effect arises between TMS airflow and inlet duct drag. When the TMS is optimised in isolation, it has no incentive to limit the heat exchanger frontal area, since the aerodynamic penalty of a bulky inlet resides in a downstream discipline. The sequential optimiser therefore saturates both the cooling-air mass flow and the coolant flow rates, producing a deep, narrow heat exchanger with large volume. The coupled optimiser, which sees inlet mass and drag as part of the shared objective, reduces cooling airflow and selects a wide, shallow heat exchanger geometry. In this formulation, the aerodynamic drag penalty of the inlet duct enters the objective function directly as a propulsive fuel penalty, computed from the additional shaft power required to overcome the inlet-induced drag increment over the design mission. This ensures that the optimiser simultaneously weighs the powertrain mass of the inlet against its aerodynamic cost, rather than treating them as independent contributions. As a result, the coupled solution reduces the inlet mass from 10.7 kg to 5.4 kg and the external drag increment from 17 N to 13 N, contributing an additional saving of 5.3 kg at system level.

Introducing drag feedback through a second sequential pass not only fails to recover the optimality gap, but amplifies it, revealing a self-reinforcing coupling cascade. The oversized heat exchanger selected in the first pass generates a non-negligible external drag increment of 16.8 N. When this is fed back as an additional shaft power requirement, the motor and fuel cell optimisers must size for a slightly higher power demand. A larger fuel cell stack operating at the same low cell voltage produces more heat, which forces the TMS optimiser to select a larger heat exchanger, increasing

the inlet drag further and closing a loop that drives component masses upward at every step. As shown in Table 2, every subsystem mass increases from the first to the second pass, with the TMS growing by 2.0 kg and the fuel-cell system by 0.9 kg, for a net system increase of 3.5 kg.
This behaviour illustrates a fundamental limitation of sequential optimisation in tightly coupled systems. Each discipline optimiser, acting rationally within its own scope, produces a locally optimal solution that inadvertently worsens the sizing conditions of every downstream discipline. Rather than converging toward the coupled optimum, the iteration drives the system along a trajectory of monotonically increasing mass: compensating for drag requires more shaft power, more shaft power requires more cooling, and more cooling generates more drag. The coupled formulation, by making all cross-discipline penalties simultaneously visible to a single optimiser, escapes this spiral entirely.

4.2 Integrated Powertrain Sizing and Mission Energy Management

The framework is applied to the full-scale replacement of one turboprop engine aboard the Dornier Do-328, a 30-passenger regional aircraft powered by two Pratt & Whitney Canada PW119B engines, each delivering 1062 kW of shaft power each through a six-blade Hartzell propeller, with a dry weight of about 410 kg. The objective is to size a hydrogen fuel cell-battery hybrid electric powertrain reproducing the performance of a single turboprop engine across a representative 280 nm range mission.

Optimal Powertrain Design

The sizing condition is take-off at sea-level at 105 KTAS, where the full 1062 kW shaft power is demanded. To provide propulsion redundancy and improve individual fuel cell stack operating conditions, the total power generation is distributed across four identical stacks connected in parallel. This configuration not only ensures continued operation in the event of a single stack failure, but also reduces the power demand on each unit, allowing the individual stacks to operate at lower current densities and more favourable electrochemical conditions than a single large stack. The optimiser selects 700 cells per stack and an active area of 680 cm^2, with the hybridisation factor converging to $HF = 0.550$: the fuel cell is responsible for 55% of the design power (584 kW), while the battery covers the remaining 45% (478 kW) at the peak demand condition.
Table 3 lists the resulting system mass from the MDO. The electric motor shows a mass of 286 kg, as direct consequence of the 1 MW shaft power requirement, followed by the battery at 405 kg, sized at this stage exclusively for peak power through the C-rate constraint. The total system mass is 1421 kg without considering hydrogen storage and battery capacity resizing.

Component	Mass (kg)
Motor	286.4
FC system (including BoP)	133.0
TMS	54.6
Battery (power-sized)	405.2
Inverter	136.9
Inlet	6.4
Total system	1421

Table 3 – System mass breakdown for the Do-328 hybrid-electric powertrain.

Battery Energy Resizing

At design point, the battery is sized for peak power, but this criterion does not guarantee adequate energy capacity for the full mission. To determine the required pack energy capacity, a reference mission simulation is first run with an unconstrained battery, allowing the dispatch law to operate freely and capturing the true energy demand of each flight phase without depletion effects. For the Do-328 sector profile, this demand is 95.902 kWh, split across take-off (19.900 kWh), climb (50.700 kWh), and the upper climb ramp (25.300 kWh). The cruise and descent phases draw nothing from the battery since they are fully covered by fuel cell.

For battery safety reasons and to prevent ageing SoC limits ($SoC_{min} = 0.20$, $SoC_{max} = 0.90$) are considered. Additionally, for extra mission safety, a 10% energy margin is added. Therefore, the required pack capacity is 150.703 kWh, scaling the battery from 405 kg to 591 kg — a 46% increase over the power-only sizing. This gap underlines a key challenge in hybrid-electric powertrain sizing: the power and energy constraints pull in opposite directions, and an MDO that optimises system mass only at the design point will systematically undersize the battery relative to the mission energy requirement. The final mass with the resized battery rises to 1607 kg.

Mission Optimisation

Figure 5 shows the mission optimisation results for the 280 nm Do-328 range. Hydrogen consumption follows a continuously increasing ramp, where no transient behaviour can be seen, extending fuel cell lifespan, as a consequence of J_{dyn} in Equation (12). Total hydrogen consumption is 57.7 kg, which with a gravimetric index of 0.30 corresponds to a hydrogen storage system of 201.8 kg. The powertrain dry mass is then 1,819 kg for a delivered shaft power of 1062 kW.

The power distribution allocates battery power as a linear fraction of the excess demand above the cruise power threshold, smoothly tapering from 478 kW at peak demand to zero at cruise entry. During take-off the fuel cell delivers 584 kW while the battery contributes the remaining 478 kW, reducing the SoC from 0.90 to 0.77 over the 150-second ground roll. Across the 10-minute climb plateau at 80% power (850 kW), the battery share falls to 304 kW and the SoC reaches 0.43 at the top of the plateau. Through the upper climb ramp, as power demand decreases, the battery contribution tapers from 152 kW to zero. The SoC arrives at FL250 at 0.264, comfortably above the 0.20 reserve floor.

During the 60-minute cruise at FL250, the fuel cell operates as the sole power source at 478 kW. This only source cruise has two advantages: the fuel cell is working at continuous power without needing extra support from the battery; and the fuel cell operates at $\sim$80% of its maximum power, which reduces its ageing and extends the fuel cell durability. Moreover, the 40.9 kg of hydrogen consumed during cruise represents 71% of the mission total, confirming that cruise efficiency dominates the system-level sizing.

5. Conclusions

This work presented a fully integrated, physics-based MDO framework for the conceptual sizing of hydrogen-fuelled plus battery electric powertrains in sustainable aviation aircraft. By simultaneously optimising the fuel cell system, electric motor, battery pack, TMS, air intake and BoP within a single gradient-based environment, the framework explicitly resolves the cross-disciplinary couplings governing hydrogen-electric propulsion performance. Those couplings are architecturally inaccessible by conventional sequential sizing procedures.

The comparison between coupled and sequential optimisation architectures on a design point for 100 kW power at sea-level provides clear quantitative evidence of these benefits. The fully coupled MDO solution achieves a total powertrain mass of 184.1 kg, representing a reduction of 35.2 kg (-19.1%) compared to the one-pass sequential approach. Critically, introducing drag feedback through a second sequential pass amplifies the mass gap to 38.7 kg ($+21.0\%$) revealing a self-reinforcing coupling cascade driven by the interaction between fuel cell operating point, waste heat generation and TMS sizing. The coupled optimiser resolves this trade-off by converging to a higher mean cell voltage ($V_{cell} = 0.538$ V vs. 0.500 V), which reduces current density and cuts heat sufficiently to shrink the heat exchanger volume by more than two thirds.

The application to a full-scale hybrid-electric replacement for one powerplant of the Dornier Do-328 regional aircraft further demonstrates the framework capability at mission-relevant scale. The optimised 1062 kW powertrain, achieves a total dry mass of 1819 kg including hydrogen storage, with a total mission hydrogen consumption of 57.7 kg over a 280 nm sector. The mission optimisation results highlight an important sizing challenge inherent to hybrid-electric architectures: peak-power sizing of the batteries at the design point systematically undersizes them for mission energy requirements. In this case a 46% increase in battery mass is required when energy constraints are enforced. This tension between power-driven and energy-driven sizing constitutes a key design driver which in-

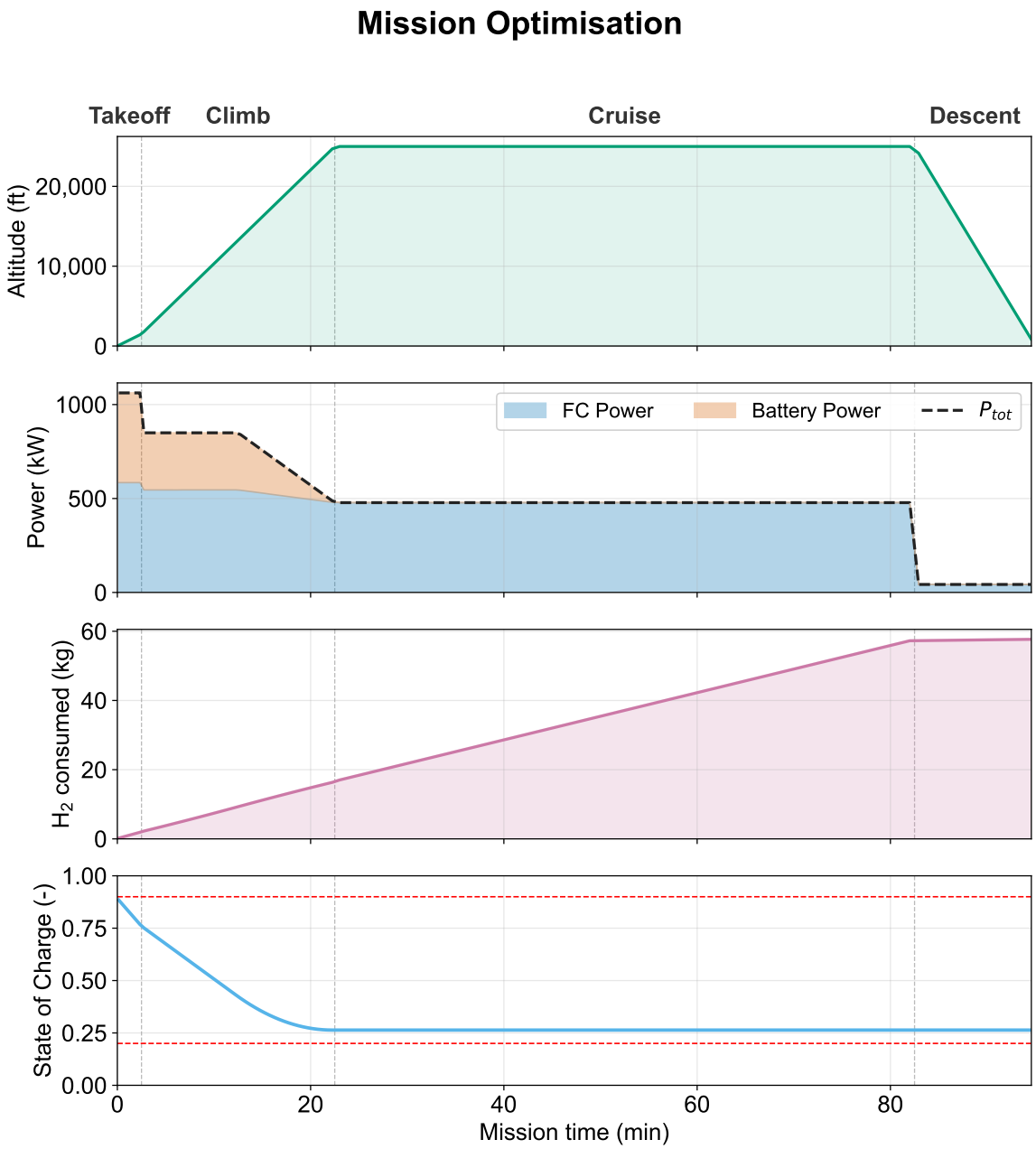


Figure 5 – Optimised mission for the Do-328 single-engine hybrid-electric replacement. Top to bottom: (1) altitude profile; (2) power split along missioned; (4) battery state of charge

tegrated MDO frameworks must explicitly capture. Additionally, results confirm that cruise efficiency dominates the system-level hydrogen consumption, accounting for 71% of total fuel consumption.
Overall, results establish that physics-based coupled optimisation is not merely preferable but necessary for hydrogen-electric powertrain design. The non-intuitive trade-offs between fuel cell efficiency, thermal rejection and aerodynamic drag penalties are invisible to decoupled methods, leading to systematically suboptimal and potentially infeasible designs.
Future work will focus on extending the framework to multi-point and mission-level design variables. Integration of certification requirements and airworthiness constraints will also be pursued to bring the framework closer to regulatory-compliant preliminary design practice.

Acknowledgements

This work has received funding from the **ODE4HERA** project, financed by the European Commission Clean Aviation Joint Undertaking under the Grant Agreement **101140510**. Views and opinions expressed are, however, those of the authors only and do not necessarily reflect those of the European Commission, the Research Executive Agency, or the European Union. Neither the European Union nor the granting authority can be held responsible for them.

Copyright Statement

The authors confirm that they, and/or their company or organisation, hold copyright on all of the original material included in this paper. The authors also confirm that they have obtained permission, from the copyright holder of any third party material included in this paper, to publish it as part of their paper. The authors confirm that they give permission, or have obtained permission from the copyright holder of this paper, for the publication and distribution of this paper as part of the ICAS proceedings or as individual off-prints from the proceedings.

References

[1] Adler E. J. and Martins J. R. R. A. Hydrogen-powered aircraft: Fundamental concepts, key technologies, and environmental impacts. *Progress in Aerospace Sciences*, 141:100922, 2023.

[2] United Nations. Paris agreement, Dec 2015. Adopted Dec. 12, 2015, T.I.A.S. No. 16-1104.

[3] Bradley M. K. and Droney C. K. Subsonic ultra green aircraft research phase ii: N+ 4 advanced concept development. Technical report, National Aeronautics and Space Administration, Langley Research Center, 2012.

[4] Brelje B. J. and Martins J. R. R. A. Electric, hybrid, and turboelectric fixed-wing aircraft: A review of concepts, models, and design approaches. *Progress in Aerospace Sciences*, 104:1–19, 2019.

[5] Trainelli L., Riboldi C. E. D., Salucci F., Rolando A. L. M., et al. A general preliminary sizing procedure for pure-electric and hybrid-electric airplanes. In *1st Aerospace Europe Conference (AEC 2020)*, pages 1–10, 2020.

[6] Gray J. S., Hwang J. T., Martins J. R. R. A., Moore K. T., and Naylor B. A. Openmdao: An open-source framework for multidisciplinary design, analysis, and optimization. *Structural and Multidisciplinary Optimization*, 59(4):1075–1104, 2019.

[7] Bahrs V., Staggat M., and Enghardt L. *Analytical model for electric machine sizing in electrified aviation*. Deutsche Gesellschaft für Luft-und Raumfahrt-Lilienthal-Oberth eV, 2022.

[8] Müller G., Vogt K., and Ponick B. *Berechnung elektrischer maschinen*. John Wiley & Sons, 2012.

[9] O'Hayre R., Cha S. W., Colella W., and Prinz F. B. *Fuel cell fundamentals*. John Wiley & Sons, 2016.

[10] Datta A. Pem fuel cell model for conceptual design of hydrogen evtol aircraft. Technical Report NASA/CR-20210000284, NASA Ames Research Center, January 2021.

[11] Schröder M., Becker F., and Gentner C. Optimal design of proton exchange membrane fuel cell systems for regional aircraft. *Energy Conversion and Management*, 308:118338, 2024.

[12] Zhang Y., Hu Z., Xu L., Liu H., Ye K., Li J., and Ouyang M. Fuel cell system for aviation applications: Modeling, parameter sensitivity, and control. *Energy Conversion and Management*, 312:118555, 2024.

[13] Doyle M., Fuller T. F., and Newman J. Modeling of galvanostatic charge and discharge of the lithium/polymer/insertion cell. *Journal of the Electrochemical society*, 140(6):1526–1533, 1993.

[14] Pornet C. and Isikveren A. T. Conceptual design of hybrid-electric transport aircraft. *Progress in Aerospace Sciences*, 79:114–135, 2015.

[15] Ragone D. V. Review of battery systems for electrically powered vehicles. Technical report, SAE Technical Paper, 1968.

[16] Xue N., Du W., Gupta A., Shyy W., Marie Sastry A., and Martins J. R. R. A. Optimization of a single lithium-ion battery cell with a gradient-based algorithm. *Journal of The Electrochemical Society*, 160(8):A1071–A1078, 2013.

[17] Peukert W. Über die abhängigkeit der kapazität von der entladestromstärke bei bleiakkumulatoren. *Elektrotechnische Zeitschrift*, 20(1897), 1897.

[18] Vratny P. C., Gologan C., Pornet C., Isikveren A. T., and Hornung M. Battery pack modeling methods for universally-electric aircraft. In *4th CEAS Air & Space Conference*, pages 525–535. Linköping Univ. Electronic Press, Linköping Sweden, 2013.

[19] Dever T. P., Duffy K. P., Provenza A. J., Loyselle P. L., Choi B. B., Morrison C. R., and Lowe A. M. Assessment of technologies for noncryogenic hybrid electric propulsion. Technical report, NASA, 2015.

[20] Glauert H. Airplane propellers. In Durand W. F., editor, *Aerodynamic Theory*, volume IV. Springer, Berlin, 1935.

[21] Leishman J. G. *Principles of Helicopter Aerodynamics*. Cambridge University Press, Cambridge, 3rd edition, 2016.

[22] Martínez-Muriel C. NFoil. GitHub Repository, 2026. https://github.com/cayetanomarmur/NFoil - Accessed: 14/05/2026.

[23] Corrigan J. J. and Schillings J. J. Empirical model for stall delay due to rotation. In *Proceedings of the AHS Aeromechanics Specialists Conference*, San Francisco, 1994.

[24] Okulov V. L. and Sørensen J. N. Maximum efficiency of wind turbine rotors using Joukowsky and Betz approaches. *Journal of Fluid Mechanics*, 649:497–508, 2010.

[25] Brelje B. J., Jasa J. P., Martins J. R. R. A., and Gray J. S. Development of a conceptual-level thermal management system design capability in openconcept. In *Proceedings of the NATO Research Symposium on Hybrid/Electric Aero-Propulsion Systems for Military Applications (AVT-RSY-323), Trondheim, Norway*, pages 07–09. North Atlantic Treaty Organization—Science and Technology Organization . . . , 2019.

[26] Incropera F. P., DeWitt D. P., Bergman T. L., and Lavine A. S. *Fundamentals of Heat and Mass Transfer*. John Wiley & Sons, 6th edition, 2007.

[27] Kays W. M. and London A. L. *Compact Heat Exchangers*. McGraw–Hill, 3rd edition, 1984.

[28] Manglik R. M. and Bergles A. E. Heat transfer and pressure drop correlations for the rectangular offset strip fin compact heat exchanger. *Experimental thermal and fluid science*, 10(2):171–180, 1995.

[29] von Mises R. *Theory of Flight*. McGraw-Hill, New York, 1945.

[30] Anderson J. D. *Modern Compressible Flow: With Historical Perspective*. McGraw-Hill, New York, 3rd edition, 2003.

[31] Goldsmith E. L. and Seddon J., editors. *Practical Intake Aerodynamic Design*. AIAA Education Series. American Institute of Aeronautics and Astronautics, Washington, D.C., 1993.

[32] Zucrow M. J. and Hoffman J. D. *Gas Dynamics*, volume 1. Wiley, New York, 1976.

[33] White F. M. *Fluid Mechanics*. McGraw-Hill, New York, 7th edition, 2011.

[34] Raymer D. *Aircraft design: a conceptual approach*. American Institute of Aeronautics and Astronautics, Inc., 2006.

[35] International Civil Aviation Organization. *Manual of the ICAO Standard Atmosphere*. International Civil Aviation Organization, Montréal, Canada, 3rd edition, 1993.

[36] Paganelli G., Delprat S., Guerra T. M., Rimaux J., and Santin J. J. Equivalent consumption minimization strategy for parallel hybrid powertrains. In *IEEE vehicular technology conference*, volume 4, pages 2076–2081, 2002.